

1 **Turbulent heat transfer as a control of platelet ice growth in**  
2 **~~supercool~~supercooled under-ice ocean boundary-layers**

3  
4 **M.G. McPhee<sup>1</sup>, C.L. Stevens<sup>2,3</sup>, I.J. Smith<sup>4</sup> and N.J. Robinson<sup>2</sup>**

5 [1] McPhee Research Company, Naches Washington, USA.

6 [2] National Institute for Water and Atmospheric Research, Greta Point Wellington, New  
7 Zealand.

8 [3] University of Auckland, Dept. Physics, New Zealand

9 [4] University of Otago, Dept. Physics, New Zealand.

10 Correspondence to: C.L. Stevens NIWA 301 Evans Bay Pde, Kilbirnie PO Box 14-901, 6021,  
11 New Zealand (c.stevens@niwa.co.nz)

## Abstract

Late winter measurements of turbulent quantities in tidally modulated flow under land-fast sea ice near the Erebus Glacier Tongue, McMurdo Sound, Antarctica, identified processes that influence growth at the interface of an ice surface in contact with ~~supereool~~supercooled seawater. The data ~~suggest~~show that turbulent heat exchange at the ocean-ice boundary is characterized by the product of friction velocity and (negative) water temperature departure from freezing, analogous to similar results for moderate melting rates in seawater above freezing. Platelet ice growth appears to increase the hydraulic roughness (drag) of fast ice compared with undeformed fast ice without platelets. ~~We hypothesize that p~~Platelet growth in ~~supereool~~supercooled water under thick ice ~~is~~appears to be rate-limited by turbulent heat transfer and that this is a significant factor to be considered in mass transfer at the under-side of ice shelves and sea ice in the vicinity of ice shelves.

## 1 Introduction

In addition to seaward advection, calving and basal melting, the distribution of mass in ice shelves depends on the so-called ice pump (Lewis and Perkin, 1986). By this mechanism, water warmer than the in situ freezing point temperature, typically High Salinity Shelf Water entering the under-shelf cavity, encounters glacial ice at ~~or near, high pressures, e.g., near the~~ grounding line. ~~The, where it is local~~ cooling~~ing~~ and freshen~~ing~~ by basal melting (~~BM~~, Figure 1) of the ice shelf underside all happens at high local pressure. The resultant buoyant water circulates to lower pressure regions as the glacier base thins toward the terminus, and in the process may become ~~supereool~~supercooled relative to its in situ pressure (Foldvik and Kvinge, 1974). Supercooled Ice Shelf Water (ISW) is formed. ~~Supereool~~Supercooled water can then deposit ice by direct growth of ice crystals attached at the ice underside, or by upward migration

1 of frazil crystals suspended by turbulence in the water [\(Dieckmann et al 1986\)](#). In this way,  
2 fresh glacial ice near the grounding line transforms to marine ice (Langhorne 2008). Evidence  
3 from icebergs (Kipfstuhl et al., 1992), borehole (Craven, et al., 2005) and radar studies  
4 (Engelhardt and Determann, 1987; Robin et al., 1983; Holland, et al., 2009) indicate that marine  
5 ice can reach appreciable thicknesses, and that the ice pump is active under shelves where the  
6 water entering the cavity is near freezing.

7 Formation of marine ice ~~([ML-Figure 1](#))~~[\(Figure 4\)](#) under ice shelves is difficult to observe  
8 directly (Craven et al. 2015), but similar effects are readily observed beneath nearby sea ice  
9 (e.g. Robinson et al., 2014; Hoppmann et al. 2015; Langhorne et al. 2015; Hughes et al. 2015).  
10 For example in McMurdo Sound, Antarctica, sea ice crystals that have formed in  
11 ~~superecools~~[supercooled](#) water have been observed and reported since the British National  
12 Antarctic (Discovery) Expedition of 1901–04 (Hodgson, 1907) and the British Antarctic (Terra  
13 Nova) Expedition of 1910–1913 (Wright and Priestley, 1922). Crystals observed in McMurdo  
14 Sound have reported to be up to 250 mm in diameter (Robinson et al, 2014; Smith et al., 2001).  
15 In part because of their size [and aspect ratio, and that turbulent suspension is not a direct driver,](#)  
16 these crystals are ~~now known~~[identified](#) as “platelet ice”. They have been observed attached to  
17 the underside of sea ice (Gow et al., 1998), often forming layers 2–3 m thick (Dayton et al.,  
18 1969) and in some places as much as 8 m thick (Hughes et al. 2014). Platelet ice crystals have  
19 been observed to become incorporated into the sea ice by subsequent congelation growth  
20 (Jeffries et al., 1993).

21 The presence of ~~superecools~~[supercooled](#) water measured below sea ice (Lewis and  
22 Perkin, 1985; Smith et al., 2001), and the abundance of platelet ice, has been linked to locations  
23 of observed supercooling (Crocker and Wadhams, 1989) and to the ocean currents from beneath  
24 the ice shelf (Leonard et al., 2011; Fer et al. 2012). Evidence of this link is provided by the

1 thicker accumulations of platelet ice (i.e. a sub-ice platelet layer ~~PL-Figure 1~~Figure 1) found on  
2 the western side of McMurdo Sound (Dempsey et al., 2010; Hughes et al., 2014; Robinson et  
3 al., 2014), compared to that ~~than~~ on the east (Gow et al., 1998; Jeffries et al., 1993, Dempsey  
4 et al., 2010) where platelet ice only starts to form in late winter (Paige, 1966). Leonard et al.  
5 (2006) and Mahoney et al. (2011) reported acoustic and video evidence that platelet ice crystals  
6 begin as small crystals (2-20 mm) that become larger once attached to the sea ice cover above.

7 Based on heat and mass balance measurements within the ice column, the residual  
8 oceanic heat flux associated with incorporated platelet ice has been reported as negative (i.e.,  
9 heat moves downwards into the ocean) by several authors (Gough et al., 2012; Purdie et al.,  
10 2006; Smith et al., 2012; 2015) with values of as large as ~~30~~  $\text{W m}^{-2}$  or more reported ~~elsewhere~~  
11 (Purdie et al., 2006; Smith et al., 2001). Smith et al. (2001) noted that forced convection was  
12 needed to account for the amount of platelet ice observed in McMurdo Sound, and Smith et al.  
13 (2001) and Stevens et al. (2009) estimated kinematic eddy viscosities of  $2 \times 10^{-5} \text{ m}^2 \text{ s}^{-1}$  and  
14  $5 \times 10^{-4} \text{ m}^2 \text{ s}^{-1}$ , respectively, in supercool water in McMurdo Sound. Smith et al. (2012) observed  
15 episodic growth of individual platelet ice crystals, with periods of growth at least an order of  
16 magnitude faster than the growth of the bulk sea ice. They suggested that variable currents were  
17 responsible for the episodic nature of the crystal growth. The appearance of these supercooling-  
18 induced crystals is not limited to the western margin of the Ross Ice Shelf, with observations  
19 made in other cold-cavity systems sampled to date (Dieckmann et al. 1986; Craven et al. 2014;  
20 Hoppmann et al. 2015; Langhorne et al. 2015).

21 The ~~presentis~~ work seeks to answer the questions (i) if and how the growth of platelet  
22 ice at a ~~supereool~~ supercooled ice-ocean interface impacts the physical characteristics of the  
23 interface, including hydraulic roughness and the rate of heat transfer in the water column, and  
24 (ii) what feedbacks might exist. Direct turbulence measurements make this possible by

enabling characterisation of the boundary-layer and direct measurement of heat fluxes. This facilitates improved parameterization of exchange processes in terms of mean quantities and will enhance the modeling of the ice-pump deposition phase in ice shelf cavities (Gwyther et al 2015) as well as estimation of the spatial envelope of sea ice growth influenced by these cavities (Langhorne et al. 2015).

## 2 Methods

### 2.1 Field camp and instrumentation

In October and November, 2010, the New Zealand National Institute Water and Atmospheric Research (NIWA) established a temporary station (Erebus Field Camp -- EFC) on fast (immobile) sea ice near Erebus Glacier Tongue (EGT) in McMurdo Sound, Antarctica. The general layout of EFC and its location relative to nearby geographic features is described by Stevens et al. (2014) (Figure 2). Included in the deployment was instrumentation designed to accurately measure current, temperature, and salinity in tidal flow beneath the stationary sea ice, at a resolution sufficiently small to enable turbulent fluxes of momentum, heat, and salt to be quantified.

A top-mounted mooring was deployed in 350 m of water, 2.5 km to the SW of the EFC at 77° 42.7730 S, 166° 21.4350 E, spanning the period in question. This mooring contained three Aanderaa RCM-9 units coupled with SBE 37 Microcat temperature, salinity, and pressure recorders (Seabird Electronics, USA). The current meter/Microcat pairs were located at depths of 50, 150, and 300 m. Upon recovery of the mooring it was found that the line had lifted sufficiently so that the top 10 m had frozen into the growing sub-ice platelet layer. This has been encountered previously on instrument deployments when the buoyancy force from platelet

accretion on mooring lines had overwhelmed the mooring ballast. The remote nature of the field camp meant it was not possible to deploy very heavy ballast blocks.

Flux measurements near the ice/ocean interface were made with turbulence instrument clusters (TICs), each comprising an acoustic-Doppler velocimeter (Sontek ADVOcean, 5 MHz), mounted with its fixed sample volume in the same plane as a nearby Sea-Bird Electronics temperature (SBE 3F)/conductivity (SBE 4) pair. Conductivity measurements were supplemented by a dual electrode microstructure conductivity instrument (SBE 7). The velocity sensors have a resolution of  $0.1 \text{ cm s}^{-1}$  and an accuracy of  $\pm 1\%$  of measured velocity. The dynamic range of the conductivity signal is typically large relative to instrument sensitivity with an initial accuracy of  $\pm 0.0003 \text{ S m}^{-1}$ . The thermometers have an initial accuracy of  $\pm 0.001 \text{ }^{\circ}\text{C}$  and a stability  $0.002 \text{ }^{\circ}\text{C}$  per year typically along with a self-heating error  $<0.0001 \text{ }^{\circ}\text{C}$  in still water. Here we assume a working accuracy for the temperature sensors of 5 mK. TICs configured as above have been deployed under ice during several previous projects (McPhee, 2008a; MCPhee et al., 2008; MCPhee et al., 2013; Sirevaag et al., 2010) and shown to measure well into the inertial subrange of the turbulent kinetic energy spectrum, hence adequately capturing the covariance of vector and scalar variables in turbulent flows.

The TICs were deployed on separate suspended masts ([Figure 2](#)) under fast sea ice about 2.15 m in initial thickness. Mast A included two TICs mounted 1 and 3 m below the ice on a fixed mast suspended through a 1 m diameter hole, located about 140 m from the edge of EGT. Mast B, located closer (40 m) to the glacier tongue, included two TICs mounted 4 m apart on a rigid mast that could be lowered by cable to depths up to 70 m.

## 2.2 Turbulence analysis

Time series of three velocity components, temperature, and salinity derived from

1 temperature and conductivity were segmented into 15-min realizations for calculating  
2 turbulence statistics, including the rate of dissipation of turbulent kinetic energy  $\epsilon$ , following  
3 the method described by McPhee (2008a). Currents averaged over each realization were rotated  
4 into a reference frame such that mean vertical and cross-stream horizontal components  
5 vanished, from which the velocity perturbation components were resolved ( $u'$ ,  $v'$  and  $w'$ ).  
6 Linear trends were then removed, then “area-preserving” (weighted) spectra were calculated,  
7 and transformed to the wave-number (spatial) domain under the frozen field hypothesis. Ice  
8 nucleation on instruments immersed in ~~supercool~~-supercooled water significantly degraded  
9 their performance after just a few tidal cycles. This can affect both ADVs and conductivity  
10 sensors. We used the criteria identified in McPhee et al. (2013) to remove affected data. Ice  
11 accreting on the ADV hydrophones increased noise at higher frequencies, eventually leading to  
12 ~~nonsensical~~-incorrect velocities. Consequently, we placed added emphasis on ensuring that  
13 turbulent spectra exhibited key elements including a peak in the area-preserving spectrum of  
14 vertical velocity variance and a reasonable fall-off to the -2/3 slope in the log-log representation  
15 of the area-preserving spectrum (McPhee, 1994; 2008a). Each 15 minute spectrum was  
16 evaluated for a discernible peak in the area- preserving vertical velocity variance spectrum, and  
17 if found to be viable, was included in a three-hour grouping of realizations to determine  
18 mean statistics.

19 Friction speed,  $u_*$ , (the square root of kinematic Reynolds stress magnitude) was  
20 estimated by averaging covariance statistics, i.e.,

$$u_* = \left( \langle u'w' \rangle^2 + \langle v'w' \rangle^2 \right)^{1/4} \quad (1)$$

22 where we have invoked Taylor’s frozen field hypothesis linking measurements in the time  
23 domain at a single location to ensemble statistics. After identifying the peak in each spectrum,  
24 a high-order polynomial was fitted to wavenumbers in its vicinity, which was then analyzed to

Formatted: Font: Symbol

determine the wavenumber where the negative slope reached or exceeded 2/3, taken as signifying spectral levels in the inertial subrange. The turbulent kinetic energy (TKE) dissipation rate was estimated from [\(see e.g. Tennekes and Lumley, 1972\)](#)

$$\epsilon^{2/3} = \frac{3}{4\alpha_\epsilon} S_{ww}(k) k^{5/3} \quad (2)$$

where  $S_{ww}$  is the spectral density evaluated at angular wave number  $k$ , in the inertial subrange, and  $\alpha_\epsilon$  is the Kolmogorov constant for the along-stream spectrum (0.51).

By assuming that flow within 1 m of the boundary lies within the so-called surface layer, where stress is nearly constant and the velocity profile is logarithmic, then TKE production rate by current shear is

$$P_s = \tau \frac{\partial u}{\partial z} = \frac{u_*^3}{\kappa |z|} \quad (3)$$

where  $\kappa$  is Kàrmàn's constant (0.4). [It is possible that buoyancy effects are also contributing to the turbulence and this can be examined by comparing production and dissipation rates.](#)

### 3 Results

The present data come from [the “springs” period of the spring-neap tidal cycle](#) (Figure 3a) [in order to experience the widest range of flow speeds](#), although the tidal ~~flow effect~~ is only weakly manifest in the far-field thermal structure (Figure 3b). No data were retrieved from this [far-field](#) mooring at depths shallower than 50 m due to platelet growth effects. Indeed, as well as the incorporation of the upper 10 m of the instrumented mooring line into the growing sea ice, the mooring line itself was subject to ice accumulation-driven buoyancy-driven rise of 8 m in a 50 day period although the lift was only around 1 m during the collection of the data in



(Figure 3). The 50 m data remain around  $-1.91$  to  $-1.92$  °C.

At the mast site, during the measurement period, profiles made with the mobile TIC  
mast B indicated that the water column was isothermal to about 40 m. In addition data described  
in Stevens et al (2014) from the same campaign support the contention that, to within  $\pm 5$  mK,  
the upper 40 m was isothermal. the water column was isothermal to about 40 m depth, with  
the upper 15 m exhibited temperatures below the pressure-dependent freezing temperature,  
i.e., in-situ supercool, ~~down to about 15 m~~. The growth of ice on the far-field mooring was  
corroborated by platelet growth on the cable suspending Mast B. At Mast A (TICs at 1 and 3 m  
below the ice undersurface) ice accretion on the instruments limited the duration of acceptable  
measurements to about two diurnal cycles ( $\sim 60$  h) ending early (UT) on DOY (day of year)  
301. Shortly afterwards, Mast A was recovered, and thereafter Mast B was generally stationed  
below the ~~supercool~~ supercooled zone at depths ranging from 18 to 62 m, so as to minimize ice  
accretion. Here we emphasize data from Mast A to address conditions near the horizontal fast  
ice/ocean interface.

~~Spring tide~~ Data recorded during spring tides provide the largest velocity range and  
also the largest horizontal advection of different water masses. Currents measured 1 m below  
the ice/water boundary at Mast A from late on 25 Oct 2010 (DOY 298) to early on 28 Oct  
(Figure 4a) show a significant tidal signal resulting in speeds up to around  $0.15 \text{ m s}^{-1}$ . This is  
superimposed upon a steadier westward flow strong enough to prevent current reversal (Figure  
4b) either through flow rectification or regional circulation (Stevens et al. 2014). This was  
confirmed over a 10-day period beginning ~~with on DOY 300~~ on DOY 300, where currents measured in  
the upper 60 m of the water column at the Mast B site ranged from  $0.03$  to  $0.28 \text{ m s}^{-1}$  westward  
(Stevens et al. 2014). Salinity shows a slowly increasing trend of around  $0.0075 \text{ PSU/day}$  that  
is interrupted briefly ~~at slack water~~ during low flows ("slack water") at high and low tide (Fig.

Formatted: Normal, Left, Line spacing: Double

Formatted: Indent: First line: 1.27 cm

4c). In near-freezing waters, salinity dominates ~~influence on~~ buoyancy and so these perturbations are likely some form of propagating feature in the density structure. Certainly, the features in salinity at DOY 299.3-299.5 coincide with the directional change in Fig. 4b. Temperature measurements (Fig. 4d) on the other hand do not have obvious signatures connected to the flow. This is not uncommon at these temperatures where there is almost no thermal contribution to density. The record shows that water 1 m below the ice remained, on average, 8.7 mK below freezing. The salinity trend's influence on the freezing point is apparent in Figure 4d. This trend is largely mirrored in the measured temperature.

Consideration of the turbulent properties in the measurement volume indicates that the three-hour-average estimates of rate of dissipation of turbulent kinetic energy  $\epsilon$  compares closely to ~~with the~~ production  $P_s$  (~~Figure 5~~~~Figure 5a~~). The only departure from this is for a slack--water low flow period (DOY 300.2-300.6) when the production estimate drops significantly below the dissipation rate estimate. Under-ice measurements have shown close correspondence between the dominant turbulence length scale and the inverse of the angular wavenumber at the peak of the vertical velocity variance spectrum, i.e.,  $\lambda = c_\lambda / k_{\max}$ , where  $c_\lambda$  is a constant of order unity (McPhee, 2008a; MCPhee and Martinson, 1994). A time series of  $\lambda$  is compared with the geometric (surface layer) scale  $\kappa|z|$  in ~~Figure 5~~~~Figure 5b~~ which one would expect to be a limiting scale on the turbulent eddies. The inverse peak wavenumber turbulence lengthscale sits mostly beneath the geometric scale.

When TKE production and dissipation rates are comparable, as suggested by Figure 5a, the steady, horizontally homogeneous TKE equation provides an independent estimate of friction speed based exclusively on characteristics of the vertical velocity variance spectrum

$$u_{*e} = (k_{\max} \epsilon / c_\lambda)^{1/3} u_* = \lambda \epsilon = \frac{c_\lambda}{k_{\max}} \epsilon \quad (4)$$

The virtually-independent estimates of friction speed (Figure 5c) agree well. This supports the hypothesis that buoyancy-induced turbulence is minimal in the present conditions.

The vertical turbulent heat flux can be estimated from

$$H_f = \rho c_p \langle w'T' \rangle \quad (5)$$

where  $\rho$  is water density and  $c_p$  is specific heat of seawater at constant pressure (Figure 6a). Heat flux measurements derived in such a way (Figure 6a) remain entirely negative with the standard deviation being around half the mean value. The heat flux follows a weakly diurnal pattern with broad similarity to  $u_*$  (Fig. 5c). The implication then is that a bulk description may be useful as employed for moderate melt rates in water above freezing, so that

$$H_f = \rho c_p c_H u_* \Delta T \quad (6)$$

where  $\Delta T = T - T_f(S, p)$  is the departure from the freezing temperature. The  $\Delta T$  (Figure 6b), is semidiurnal in structure and so not particularly coupled with the diurnal cycle seen in the calculated and measured heat fluxes (Fig. 6a and c). The departure from the freezing point temperature also exhibits the trend of becoming larger (i.e., increasingly negative) with time during the observation period (Figure 6a,c), and has a negatively increasing trend. Unlike the heat flux estimate, the variability around the mean is reduced. The relationship can be restructured to solve for the transfer coefficient  $c_H$ . Averaging the ratio from each of the acceptable 3-hour averages results in  $c_H = 0.0085$ . Applying this average bulk transfer coefficient and comparing with the measured (Figure 6C) indicates that the bulk approach does reasonable well. Notably, the diurnal cycle, while not apparent in the semidiurnal  $\Delta T$ , is sufficiently strongly manifest in the  $u_*$ .

Formatted: Font: (Default) Times New Roman, Check spelling and grammar

Formatted: Font: (Default) Times New Roman, Check spelling and grammar

Formatted: Font: (Default) Times New Roman

## 4 Discussion

The questions posed in the introduction relate to how the supercooling and the modified roughness associated with the resulting crystals influence the heat flux. Equation (6) indicates that the problem, for a given temperature difference, can be reduced to a combination of the turbulent heat transfer coefficient  $c_H$  and the turbulent velocity scale. The  $c_H$  value found here is not far different from values reported for basal heat exchange in above freezing water: e.g.,  $c_H = 0.0057$  for the year-long SHEBA project in the western Arctic (McPhee, 2008a); 0.0056 for first-year ice in the Weddell Gyre (McPhee et al., 1999). Furthermore, it almost matches the  $c_H = 0.0084$  determined for rapid melting in the eastern Arctic (Sirevaag, 2009). This suggests any different behaviour in heat flux is due to the velocity structure induced by the roughness.

As identified by Gwyther et al. (2015), the roughness of the boundary affects growth in two ways. First, it influences heat transfer at the ice-ocean interface and second it alters the mixing within, and entrainment into, the basal boundary-layer (BaBL, Figure 1). While these authors note that sea ice is different to the underside of an ice shelf, it is likely that, at the boundary-layer scale, that the presence of superecool-supercooled water and platelets will generate similar effects in the two systems.

There is supercooled Ice Shelf Water (ISW) water below the crystals, and these large crystals could not appear from the smaller ISW plume, because such large crystals would be bouyant enough to leave the ISW plume (Jenkins and Bombusch 1995; Smedsrud and Jenkins 2004). They need further heat loss in situ to grow to the large sizes observed, but yet the heat flux through the thick fast ice must be small. The ocean turbulent heat flux was negative (downward) throughout the entire measurement period (Fig. 6a). Sea ice in this region typically forms as congelation ice early in the growth season, then incorporates platelet ice

Formatted: Font: (Default) Times New Roman, 12 pt

Formatted: Font: (Default) Times New Roman, 12 pt

Formatted: Font: (Default) Times New Roman, 12 pt

Formatted: Font: (Default) Times New Roman, 12 pt

Formatted: Font: (Default) Times New Roman, 12 pt

Formatted: Font: (Default) Times New Roman, 12 pt

Formatted: Font: (Default) Times New Roman, 12 pt

Formatted: Font: (Default) Times New Roman, 12 pt

1 towards the end of the growth season (e.g., Smith et al., 2001). Congelation ice grows when the  
2 latent heat released during phase change is conducted from the relatively warm ocean to the  
3 relatively cold atmosphere. In this context, relatively cold means below the freezing point  
4 temperature of seawater. Platelet ice formation occurs in supercooled seawater and when this  
5 occurs near the ice/ocean boundary, the latent heat released can either be conducted upwards  
6 through the main ice column or transported downwards by turbulent heat flux into the ocean  
7 boundary layer. The latter process of negative oceanic heat flux does not occur for congelation  
8 ice because the ocean in that case is warmer than the freezing point temperature at the ice-ocean  
9 boundary. ~~The ocean turbulent heat flux was negative (downward) throughout the entire~~  
10 ~~measurement period (Figure 6a). Sea ice typically grows in water near or slightly above~~  
11 ~~freezing, where latent heat released during phase change is balanced by upward conduction~~  
12 ~~driven by air temperatures lower than the freezing temperature of seawater. In the absence of~~  
13 ~~horizontal advection, congelation growth in water at freezing temperature requires a small~~  
14 ~~upward ocean heat flux to compensate for salt release. In contrast, platelet nucleation near the~~  
15 ~~ice/ocean boundary releases heat that must be conducted either upward in the main ice column~~  
16 ~~(perhaps against the temperature gradient within the platelet layer, PL Figure 1) or downward~~  
17 ~~by turbulent heat flux in the ocean boundary layer.~~

18 There is a growing awareness of the ubiquity of such downward heat flux conditions in  
19 the vicinity of ice shelves (Robinson et al. 2014; Craven et al., 2015; Hoppmann et al., 2015).  
20 The resistance then imposed by a stationary ice cover influenced by such crystal growth on  
21 underlying boundary-layer flow depends on the undersurface *hydraulic roughness*,  $z_0$ . For the  
22 conditions found at EGT (i.e.  $P_s \approx \varepsilon$ , undeformed, relatively uniform underice surface), we  
23 expect the flow 1 m below the interface to follow the dimensionless shear equation

$$\frac{\kappa |z|}{u_*} \frac{\partial u}{\partial z} = 1 \quad (7)$$

1 where  $U$  is mean current speed. The integral of (7) yields a logarithmic velocity profile (the  
 2 “law of the wall”) where the integration constant is  $\log z_0 = -\kappa U / u_*$ . For slow currents, the  
 3 law of the wall is not necessarily valid at 1 m (McPhee, 2008b), so we evaluated  $\log z_0$  for 3-  
 4 hour averages with current speeds  $\geq 0.05 \text{ m s}^{-1}$ . ~~For  $U$  measured at 1 m (i.e.  $\log 1 = 0$ ) the~~  
 5 average with standard deviation of the acceptable 3-hour samples was

$$6 \quad \langle \log(z_0) \rangle = -3.95 \pm 0.30 \quad (8)$$

7 The expected value for  $z_0$  is thus about 19 mm.

8 The observed  $z_0$  identified here is larger than values obtained previously from  
 9 measurements under undeformed fast ice without platelet accumulation, typically found to be  
 10 nearly hydraulically smooth, with  $z_0 \sim 10^{-5} \text{ m}$  (Crawford et al., 1999; MCPhee et al., 2008;  
 11 MCPhee et al., 2013). It is comparable to values inferred for drifting, multiyear pack ice in the  
 12 Arctic and western Weddell Sea:  $\sim 40 \text{ mm}$  (MCPhee, 2008b; Shaw et al., 2009) and is  
 13 considerably larger than first-year, drifting ice near the center of the Weddell Gyre,  $\sim 1 \text{ mm}$   
 14 (MCPhee et al., 1999).

15

## 16 5 Conclusions

17 ~~Our data show that we postulate that this~~ turbulence-enhanced transfer of ~~supercool~~  
 18 ~~supercooled~~ seawater ~~is can be~~ the source of the negative heat flux measured within the ocean  
 19 boundary layer during the present observations. Our results thus complement the negative  
 20 ocean heat flux inferred from ice measurements by, e.g., Smith et al. (2012). ~~In addition, Purdie~~  
 21 ~~et al. (2006) and Gough et al. (2012) estimated of the amount of ice growth through negative~~  
 22 ~~oceanic heat flux (Figure 7) as additional support for the contention.~~ Furthermore, the  
 23 downward ocean heat flux, which this work suggests depends on the product of friction speed

**Formatted:** Font: (Default) Times New Roman, 12 pt, Italic

**Formatted:** Font: (Default) Times New Roman, 12 pt

**Formatted:** Font: (Default) Times New Roman, 12 pt

**Formatted:** Font: (Default) Times New Roman, 12 pt, Font color: Auto

**Formatted:** Font: (Default) Times New Roman, 12 pt, Font color: Auto

**Formatted:** Font: (Default) Times New Roman, 12 pt, Font color: Auto

**Formatted:** Font color: Auto

1 and  $\Delta T$ , imposes a strong constraint on the rate of ice growth under stationary ice in ~~supercool~~  
2 supercooled water. This has significant implications for parametrization of basal boundary-  
3 layers beneath both ice shelves and sea ice (Gwyther et al 2015).

4 It is instructive to consider the heat flux distribution as a function of the  $u^*$  and  $\Delta T$   
5 drivers (~~Figure 7~~Figure 7) as there is growing evidence that the presence of ice shelves produces  
6 values for both that are outside present expectations. The heat flux contours enable  
7 contextualisation of existing results obtained either as measurements of  $u^*$  and  $\Delta T$  pairs or as a  
8 heat flux for a particular temperature condition. Parameterisation in terms of  $u^*$  suggests  
9 timescale is important. While heat flux is typically considered over daily, or longer, timescales  
10 so as to compare with seasonal ice growth,  $u^*$  will be modulated primarily by tides as direct  
11 wind forcing is effectively absent in the present fast ice situation. This is especially important  
12 if there is some non-linearity in the growth of more ice as the form of platelets influences  $u^*$ .

13 While the present short period of data saw around a factor of 6 variability in  $H_f$  (Figure  
14 6~~Figure 6~~c) as the two drivers are largely de-coupled, the contours (Figure 7) suggest show that,  
15 depending on the local turbulence conditions and degree of supercooling, this variability ~~might~~  
16 approaches two orders of magnitude. Extending this idea, Gwyther et al. (2015) presents a  
17 sensitivity analysis that suggest that the variability in  $u^*$  through platelet modification of  $C_d$   
18 might be as much as an order of magnitude. Future work to address this issue -needs to enhance  
19 our focus on understanding of quantifying the combined influence of turbulence, thermally-  
20 induced roughness and heat transfer.

## 21 **Acknowledgements**

23 The authors wish to thank Pat Langhorne for discussion and support. Tim Haskell, Brett Grant,  
24 Tim Stanton, Jim Stockel, Alex Forrest, Martin Doble and the staff of Scott Base are thanked

1 for their support in the field. Metadata are lodged with Antarctica New Zealand. The work was  
2 funded by The New Zealand Royal Society administered Marsden Fund, and USA NSF support  
3 to McPhee (ANT-0732804). Logistic support was provided by Antarctica New Zealand and  
4 the USAP.



## 1   **References**

- 2   Craven, M., Carsey, F., Behar, A., Matthews, J., Brand, R., Elcheikh, A., Hall, S., and  
3   Treverrow, A.: Borehole imagery of meteoric and marine ice layers in the Amery Ice Shelf,  
4   East Antarctica. *J. Glaciol.*, 51, 75 - 84, doi:10.3189/172756505781829511, 2005.
- 5   Craven, M., Warner, R. C., Galton-Fenzi, B. K., Herraiz-Borreguero, L., Vogel, S. W., and  
6   Allison, I.: Platelet ice attachment to instrument strings beneath the Amery Ice Shelf, East  
7   Antarctica. *J. Glaciol.*, 60, 383-393, doi:10.3189/2014JoG13J082, 2014.
- 8   Crawford, G., Padman L., and McPhee, M. G.: Turbulent mixing in Barrow Strait, *Cont. Shelf*  
9   *Res.*, 19, 205-245. doi:10.1016/S0278-4343(98)00086-7, 1999.
- 10   Crocker, G. B., and Wadhams P.: Modelling Antarctic fast-ice growth, *J. Glaciol.*, 35, 3-8,  
11   1989.
- 12   Dayton, P. K., Robilliard G. A., and DeVries A. L.: Anchor ice formation in McMurdo Sound,  
13   Antarctica, and its biological effects, *Science*, 163, 274-276, 1969.
- 14   Dempsey, D. E., Langhorne, P. J., Robinson, N. J., Williams, M. J. M., Haskell, T. G., and  
15   Frew, R. D.: Observation and modeling of platelet ice fabric in McMurdo Sound,  
16   Antarctica, *J. Geophys. Res.: Oceans*, 115(C1), doi:10.1029/2008JC005264, C01007, 2010.
- 17   Dieckmann, G., Rohardt, G., Hellmer, H. and Kipfstuhl, J.: The occurrence of ice platelets at  
18   250 m depth near the Filchner Ice Shelf and its significance for sea ice biology, Deep Sea  
19   Res., Part A, 33, 141–148, 1986.
- 20   Engelhardt, H., and Determann, J.: Borehole evidence for a thick layer of basal ice in the  
21   central Ronne Ice Shelf, *Nature*, 327(28), 318–319, 1987.
- 22   Fer, I., Makinson, K., and Nicholls, K., Observations of thermohaline convection adjacent to  
23   Brunt Ice Shelf. *J. Phys. Oceanogr.*, 42, 502-508. doi: 10.1175/JPO-D-11-0211.1, 2012.

**Formatted:** reference, Adjust space between Latin and Asian text, Adjust space between Asian text and numbers

1 Foldvik, A., and Kvinge, T.: Conditional instability of sea water at the freezing point, Deep-  
2 Sea Res. 21, 169–174 (doi:10.1016/0011-7471(74)90056-4), 1974.

3 Gough, A. J., Mahoney, A. R., Langhorne, P. J., Williams, M. J. M., Robinson, N. J., and  
4 Haskell, T. G.: Signatures of supercooling: McMurdo Sound platelet ice, J. Glaciol., 58, 38-  
5 50. doi: 10.3189/2012JoG10J218, 2012.

6 Gow, A. J., Ackley, S., and Govoni, J.W. : Physical and structural properties of land-fast sea  
7 ice in McMurdo Sound, Antarctica, Antarctic Research Series, 74, 355-374, 1998.

8 Gwyther, D. E., Galton-Fenzi, B. K., Dinniman, M. S., Roberts, J. L., and Hunter, J. R.: The  
9 effect of basal friction on melting and freezing in ice shelf ocean models. to appear in Ocean  
10 Modelling, 2015.

11 Hodgson, T. V.: On collecting in Antarctic seas Volume III Zoology and Botany, British  
12 National Antarctic Expedition, 1901–1904, Trustees of the British Musuem, London, UK, 3,  
13 1–10, 1907.

14 Holland, P. R., Corr, H. F. J., Vaughan, D. G., Jenkins, A., and Skvarca, P., Marine ice in  
15 Larsen Ice Shelf. Geophys. Res. Lett., 36, L11,604, doi:10.1029/2009GL038162, 2009.

16 Hoppmann, M., Nicolaus, M., Paul, S., Hunkeler, P. A., Heinemann, G., Willmes, S., ... &  
17 Gerdes, R. Ice platelets below Weddell Sea landfast sea ice. Annals of Glaciology, 56, 175-  
18 190, 2015.

19 Hughes, K. G., Langhorne, P. J., Leonard, G. H., and Stevens, C. L. : Extension of an Ice  
20 Shelf Water plume model beneath sea ice with application in McMurdo Sound, Antarctica,  
21 J. Geophys. Res.: Oceans, 119(12), 8662-8687. doi: 10.1002/2013JC009411, 2014.

22 Jeffries, M. O., Weeks, W. F., Shaw, R., and Morris, K.: Structural characteristics of  
23 congelation and platelet ice and their role in the development of Antarctic land-fast sea ice,

1 J. Glaciol., 39, 223-238, 1993.

2 Jenkins, A., and Bombosch A., Modeling the effects of frazil ice crystals on the dynamics and  
3 thermodynamics of the ice shelf water plumes, J. Geophys. Res., 100, 6967–6981, 1995.

4 Kipfstuhl, J., Dieckmann, G., Oerter, H., Hellmer, H., and Graf, W.: The origin of green  
5 icebergs in Antarctica, J. Geophys. Res., 97(C12), 20319–20324, 1992.

6 Langhorne, P.: Interactions between ocean, ice shelf, and sea ice. In Proceedings of the 19th  
7 International Association of Hydraulic Engineering and Research Symposium on Ice. IAHR  
8 & AIRH, Vancouver, Canada, 765-776, 2008.

9 Langhorne, P.J., Hughes, K.G., Gough, A.J., Smith, I.J., Williams, M.J.M., Robinson, N.J.,  
10 Stevens, C.L., Rack, W., Price, D., Leonard, G.H. and Mahoney, A.R.: Observed platelet ice  
11 distributions in Antarctic sea ice: An index for ocean-ice shelf heat flux. Geophysical  
12 Research Letters, 42(13), pp.5442-5451. 2015.

13 Leonard, G. H., Purdie, C. R., Langhorne, P. J., Haskell, T. G., Williams, M. J. M., and Frew,  
14 R. D.: Observations of platelet ice growth and oceanographic conditions during the winter  
15 of 2003 in McMurdo Sound, Antarctica, J. Geophys. Res.: Oceans, 111(C4), C04012,  
16 doi:10.1029/2005JC002952, 2006.

17 Leonard, G. H., Langhorne, P. J., Williams, M. J. M., Vennell, R., Purdie, C.R., Dempsey, D.  
18 E., Haskell, T. G., and Frew, R. D.: Evolution of supercooling under coastal Antarctic sea  
19 ice during winter, Antarctic Science, 23, 399-409, doi:10.1017/S0954102011000265, 2011.

20 Lewis, E. L., and Perkin, R.G. : The winter oceanography of McMurdo Sound, Antarctica,  
21 Antarctic Research Series, 43, 145-165, 1985.

22 Lewis, E. L., and Perkin, R. G.: Ice pumps and their rates, J. Geophys. Res., 91(C10), 11756-  
23 11762, 1986.

**Formatted:** reference, Adjust space between Latin and Asian text, Adjust space between Asian text and numbers

1 Mahoney, A. R., Gough, A. J., Langhorne, P. J., Robinson, N. J., Stevens, C. L., Williams,  
 2 M. J. M., and Haskell, T. G.: The seasonal appearance of ice shelf water in coastal  
 3 Antarctica and its effect on sea ice growth, *J. Geophys. Res.: Oceans*, 116(C11), C11032.  
 4 doi:10.1029/2011JC007060, 2011.

5 McPhee, M. G.: On the Turbulent Mixing Length in the Oceanic Boundary Layer, *J. Phys.*  
 6 *Oceanog.*, 24, 2014-2031, 1994.

7 McPhee, M. G.: Air-Ice-Ocean Interaction: Turbulent ocean boundary layer exchange  
 8 processes, ix, 215 p. pp., Springer, New York, 2008a.

9 McPhee, M. G. : Physics of early summer ice/ocean exchanges in the western Weddell Sea  
 10 during ISPOL, *Deep Sea Research Part II: Topical Studies in Oceanography*, 55, 1075-1097,  
 11 2008b.

12 McPhee, M. G., and Martinson, D. G.: Turbulent Mixing Under Drifting Pack Ice in the  
 13 Weddell Sea, *Science*, 263(5144), 218-221, 1994.

14 McPhee, M. G., Kottmeier, C., and Morison, J. H.: Ocean Heat Flux in the Central Weddell  
 15 Sea during Winter, *J. Phys. Oceanog.*, 29, 1166-1179, 1999.

16 McPhee, M. G., Morison, J. H., and Nilsen, F.: Revisiting heat and salt exchange at the ice-  
 17 ocean interface: Ocean flux and modeling considerations, *J. Geophys. Res.: Oceans*,  
 18 113(C6), C06014, 2008.

19 McPhee, M. G., Skogseth, R., Nilsen, F., and Smedsrud, L.H.: Creation and tidal advection of  
 20 a cold salinity front in Storfjorden: 2. Supercooling induced by turbulent mixing of cold  
 21 water, *J. Geophys. Res.: Oceans*, 118, 3737-3751. doi:10.1002/jgrc.20261, 2013.

22 Paige, R. A.: Crystallographic studies of sea ice in McMurdo Sound, *AntarcticaRep.*, 31 pp,  
 23 US Naval Civil Engineering Laboratory, Port Hueneme, California, USA, 1966.

1 Purdie, C. R., Langhorne, P. J., Leonard, G. H., and Haskell, T. G. : Growth of first-year  
2 landfast Antarctic sea ice determined from winter temperature measurements, *Annals of*  
3 *Glaciology*, 44, 170-176, 2006.

4 Robin, G. d. Q., Doake, C. S. M., Kohnen, H., Crabtree, R. D., Jordan, S. R., and Möller, D.:  
5 Regime of the Filchner-Ronne ice shelves, Antarctica, *Nature*, 302(14), 582–586, 1983.

6 Robinson, N. J., Williams, M. J. M., Stevens, C. L., Langhorne, P. J., and Haskell, T. G.:  
7 Evolution of a supercooled Ice Shelf Water plume with an actively growing subice platelet  
8 matrix, *J. Geophys. Res.: Oceans*, 119(6), 3425-3446. doi:10.1002/2013JC009399, 2014.

9 Shaw, W. J., Stanton, T. P., McPhee, M. G., Morison, J. H., and Martinson, D. G.: Role of the  
10 upper ocean in the energy budget of Arctic sea ice during SHEBA, *J. Geophys. Res.:*  
11 *Oceans*, 114(C6), C06012, 2009.

12 Sirevaag, A.: Turbulent exchange coefficients for the ice/ocean interface in case of rapid  
13 melting, *Geophys. Res. Lett.*, 36(4), L04606, 2009.

14 Sirevaag, A., McPhee, M. G., Morison, J. H., Shaw, W. J., and Stanton, T. P.: Wintertime  
15 mixed layer measurements at Maud Rise, Weddell Sea, *J. Geophys. Res.: Oceans*, 115(C2),  
16 C02009. doi: 10.1029/2008JC005141, 2010.

17 Smedsrud, L. H., and Jenkins, A., Frazil ice formation in an ice shelf water plume, J.  
18 *Geophys. Res.*, 109, C03025, doi:10.1029/2003JC001851, 2004.

19 Smith, I. J., Langhorne, P. J., Frew, R. D., Vennell, R., and Haskell, T. G.: Sea ice growth  
20 rates near ice shelves, *Cold Regions Science and Technology*, 83–84, 57-70, 2012.

21 Smith, I. J., Langhorne, P. J., Todahl, H. J., Haskell, T. G., Frew, R., and Vennell, R.:  
22 Platelets ice and the land-fast sea ice of McMurdo Sound, Antarctica, *Annals of Glaciology*,  
23 33, 21-27, 2001.

Formatted: reference, Adjust space between Latin and Asian text, Adjust space between Asian text and numbers

1 Smith, I. J., Gough, A. J., Langhorne, P. J., Mahoney, A. R., Leonard, G. H., van Hale, R.,  
2 Jendersie, S., and Haskell, T. G.: First-year land-fast Antarctic sea ice as an archive of ice  
3 shelf meltwater fluxes. *Cold Regions Science and Technology* 113, 63-70, 2015.

4 Stevens, C. L., Robinson, N. J., Williams, M. J. M., and Haskell, T. G.: Observations of  
5 turbulence beneath sea ice in southern McMurdo Sound, Antarctica, *Ocean Science*, 5, 435-  
6 445. doi:10.5194/os-5-435-2009, 2009.

7 Stevens, C. L., McPhee, M. G., Forrest, A. L., Leonard, G. H., Stanton, T., and Haskell, T. G.:  
8 The influence of an Antarctic glacier tongue on near-field ocean circulation and mixing, *J.*  
9 *Geophys. Res.: Oceans*, 119(4), 2344-2362, doi:10.1002/2013JC009070. 2014.

10 Tennekes, H., Lumley, J.L. A first course in turbulence. MIT press, 1972.

11 Wright, C. S., and Priestley, R. E.: *Glaciology – British (Terra Nova) Antarctic Expedition,*  
12 *1910–1913*, Harrison and Sons, London, U.K., 1922.

Formatted: reference

## Figures

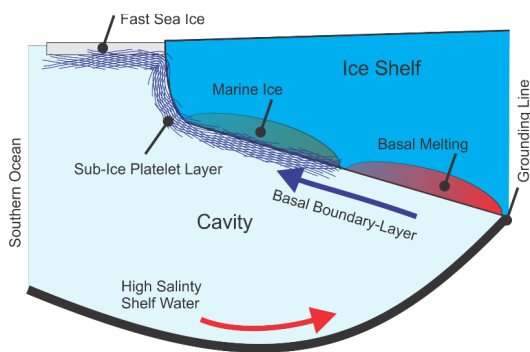


Figure 1 Ice pump showing high salinity shelf water (HSSW) flowing in at the base of an ice shelf cavity, commencing basal melting (BM) at, or around, the grounding line (GL). This buoyant meltwater flows upwards and outwards in a basal boundary-layer (BaBL). An associated platelet-forming layer (PL) supports ice growth through freezing into marine ice (MI) and PL beneath fast sea ice.

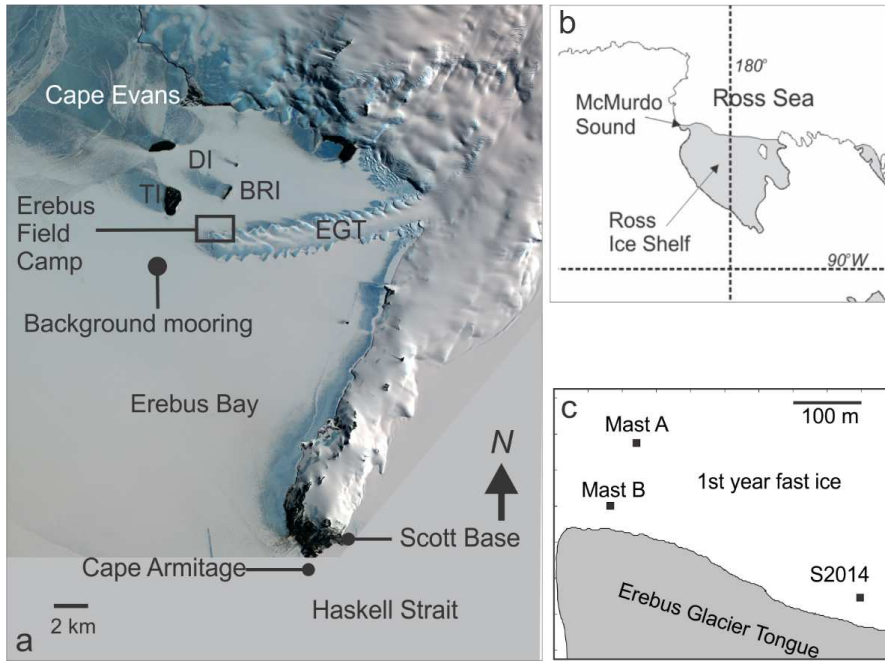


Figure 2 (a) McMurdo Sound, Antarctica, in the context of the Ross Ice Shelf and the Ross Sea. (b) SW McMurdo Sound image from ASTER (Advanced Space borne Thermal Emission and Reflection Radiometer) satellite image of south east McMurdo Sound including the Erebus glacier tongue (EGT), the Dellbridge Islands (DI), Erebus Bay (EB), Cape Evans (CE), Cape Armitage (CA), Haskell Strait (HS), Scott Base (SB), background mooring (BG) and the Erebus field camp (EFC). The Dellbridge Islands include Tent Island (TI) and Big Razorback Island (BRI). (b) The McMurdo Sound region, Antarctica, in the context of the Ross Ice Shelf and the Ross Sea. (c) Erebus Field Camp locale showing the turbulence mast locations relative to the edge of EGT.



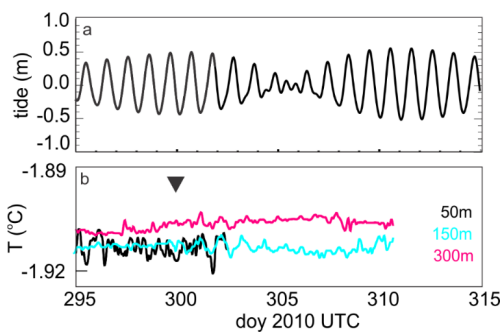
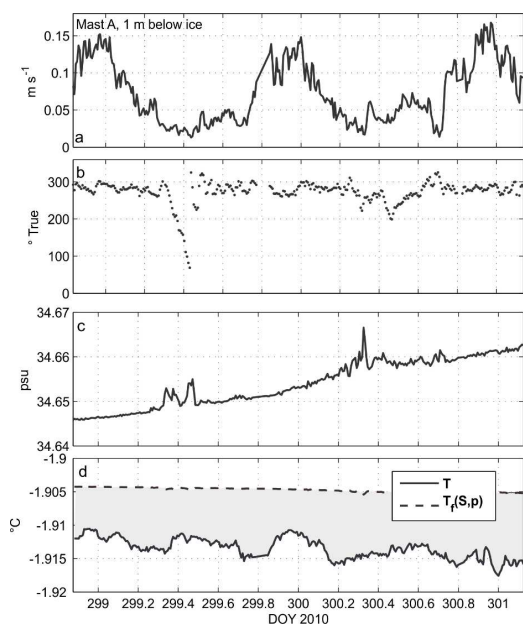


Figure 3 (a) tidal elevation and (b) in situ temperatures from background mooring (BG in [Figure 2](#)). The time of the present detailed observations are marked with the triangle in (b). The sensor at 50 m stopped early due to battery exhaustion.

1



2

Figure 4 (a) Current speed at 1 m below the ice/ocean boundary from Mast A. (b) Current direction (bearing from true north). (c) Salinity (practical salinity scale). (d) Water temperature (solid) and water freezing temperature at 2 m depth (dashed).

3

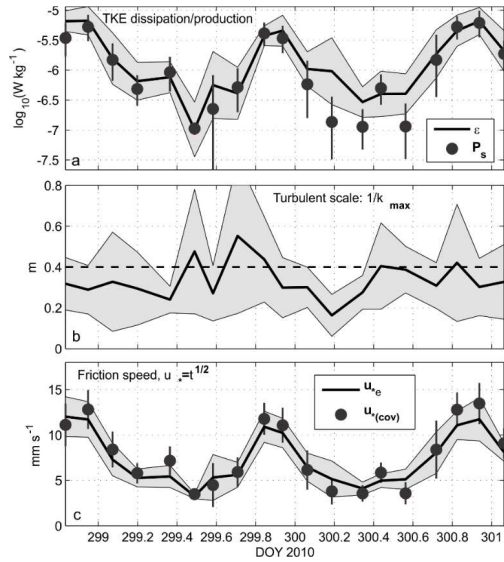
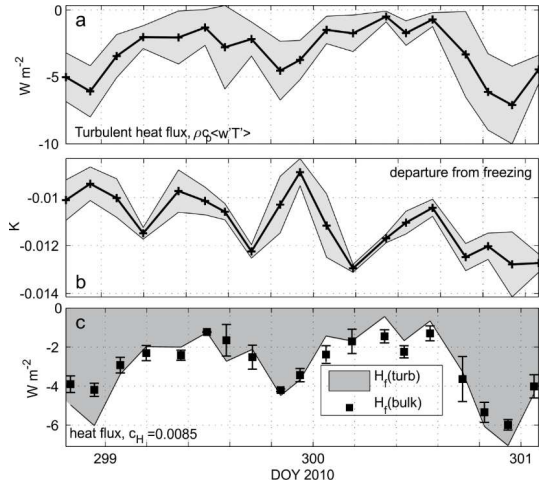


Figure 5 (a) Three-hour averages of turbulent kinetic energy dissipation rate (solid with shading showing  $\pm 1$  std. deviation of the 15-min realizations in each average) and TKE production by shear (circles with std. deviation). (b) Turbulent length scale from the inverse wavenumber at  $w$  variance spectral peaks. Dashed line indicates the “geometric” surface layer scale,  $\kappa|z|$ . (c) Independent estimates from of friction speed from  $w$  variance spectra (solid with shading) and from covariance statistics (circles with std. deviation bars).

1



2

Figure 6 (a) Three-hour averages of turbulent heat flux, solid with std. deviation shading. (b) Departure of temperature from in situ freezing point temperature. (c) Comparison showing measured heat flux (shaded) with bulk estimates based on the product of  $u_s$  and  $\Delta T$  using the transfer coefficient identified using equation (6).

3

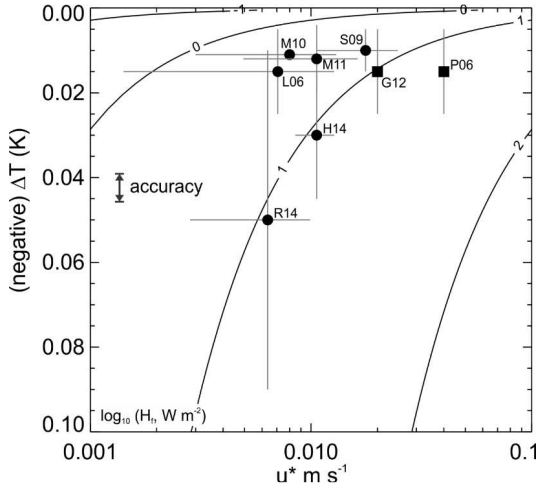


Figure 7 Contours of  $\log_{10}$  of heat flux  $H_f$ , as a function of friction speed  $u^*$  and thermal driving  $\Delta T$ , for present  $c_H$  estimate. Contours describe equation (6). Circles are from measurements of  $u^*$  and  $\Delta T$ , (L06 Leonard et al 2006; S09 Stevens et al. 2009; M11 Mahoney et al. 2011; H14 Hughes et al. 2014; R14 Robinson et al. 2014 and M10 this study). The “error-bars” represent degree of variability. The  $u^*$  were either directly measured (i.e. M10) or inferred from flow  $U$  using a drag coefficient whereby  $u^*=(C_d)^{1/2}U$ . The squares are from observations inferring heat flux so that a  $u^*$  is inferred given the observed  $\Delta T$  (P06 Purdie et al. 2006; G12 Gough et al. 2012).